

Determination of Outflow Properties for the Quasi-thermal Radiation-Dominated Gamma-Ray Bursts

XIN-YING SONG ¹, LING-JUN WANG,^{1,2} AND SHU ZHANG^{1,2}

¹*Key Laboratory of Particle Astrophysics, Institute of High Energy Physics, Chinese Academy of Sciences, Beijing 100049, China*

²*University of Chinese Academy of Sciences, Chinese Academy of Sciences, Beijing 100049, China*

ABSTRACT

Some gamma-ray bursts (GRBs) are observed with the prompt phase dominated by quasi-thermal (QT) emission. In this analysis, we focus on the QT emission which is well described by a multi-color blackbody function, rather than that with a hump-like spectrum. Based on this modeling, a characteristic temperature with the corresponding flux is taken as a probe to diagnose the magnetization properties of the central engine with the ‘top-down’ approach proposed by Gao & Zhang. Furthermore, the initial radius of the acceleration (r_0) for the outflow as well as the magnetization parameter (σ_0) could be constrained to within a narrower range than the former method (a blackbody plus non-thermal component is used in the modeling, and r_0 takes arbitrary values of $10^7 - 10^9$ cm). We apply this method to some QT-dominated bursts with known emission properties, such as GRB 210121A from a typical pure hot fireball and GRB 210610B from a hybrid jet. It is found that this method works well on these control samples, and provides more reasonable estimation and physical explanation than those with the former method. With this method, we find it is suggestive that the photospheric emission of GRB 221022B is mainly from a pure hot fireball, rather than from a hybrid jet, while the non-thermal component is caused by internal shock (IS) mechanism, due to the increasing Lorentz Factor with time.

Keywords: gamma-ray bursts

1. INTRODUCTION

The emission mechanism of gamma-ray bursts (GRBs) remains elusive despite about half a century of observation and investigation. There are two leading scenarios which have been suggested to interpret the observed spectra of GRBs. One is synchrotron radiation, which invokes a non-thermal emission of relativistic charged particles either from internal shocks (IS) or from internal magnetic dissipation processes (e.g., Lloyd & Petrosian 2000; Zhang & Yan 2011). The other is photospheric emission as a natural consequence of the fireball (e.g., Cavallo & Rees 1978; Goodman 1986; Paczynski 1986). However, the photospheric emission is not in its usual form because its spectrum is broadened. The Planck spectrum related to the photospheric emission could be broadened in two ways. First, dissipation below the photosphere can heat electrons above the equilibrium temperature. ISs below the photosphere (e.g., Rees & Mészáros 2005), magnetic reconnection (e.g., Giannios & Spruit 2005), and hadronic collision shocks (e.g., Vurm et al. 2011) have been suggested as the dissipation processes. Second, the modification of Planck spectrum could be caused by geometrical broadening. This means that the observed spectrum is a superposition of a series of blackbodies of different temperatures, arising from different angles to the line of sight. Therefore, a multi-blackbody (mBB) function could be used to describe the quasi-thermal spectrum.

The possible origins for the observed photospheric emission in GRBs are listed as bellow:

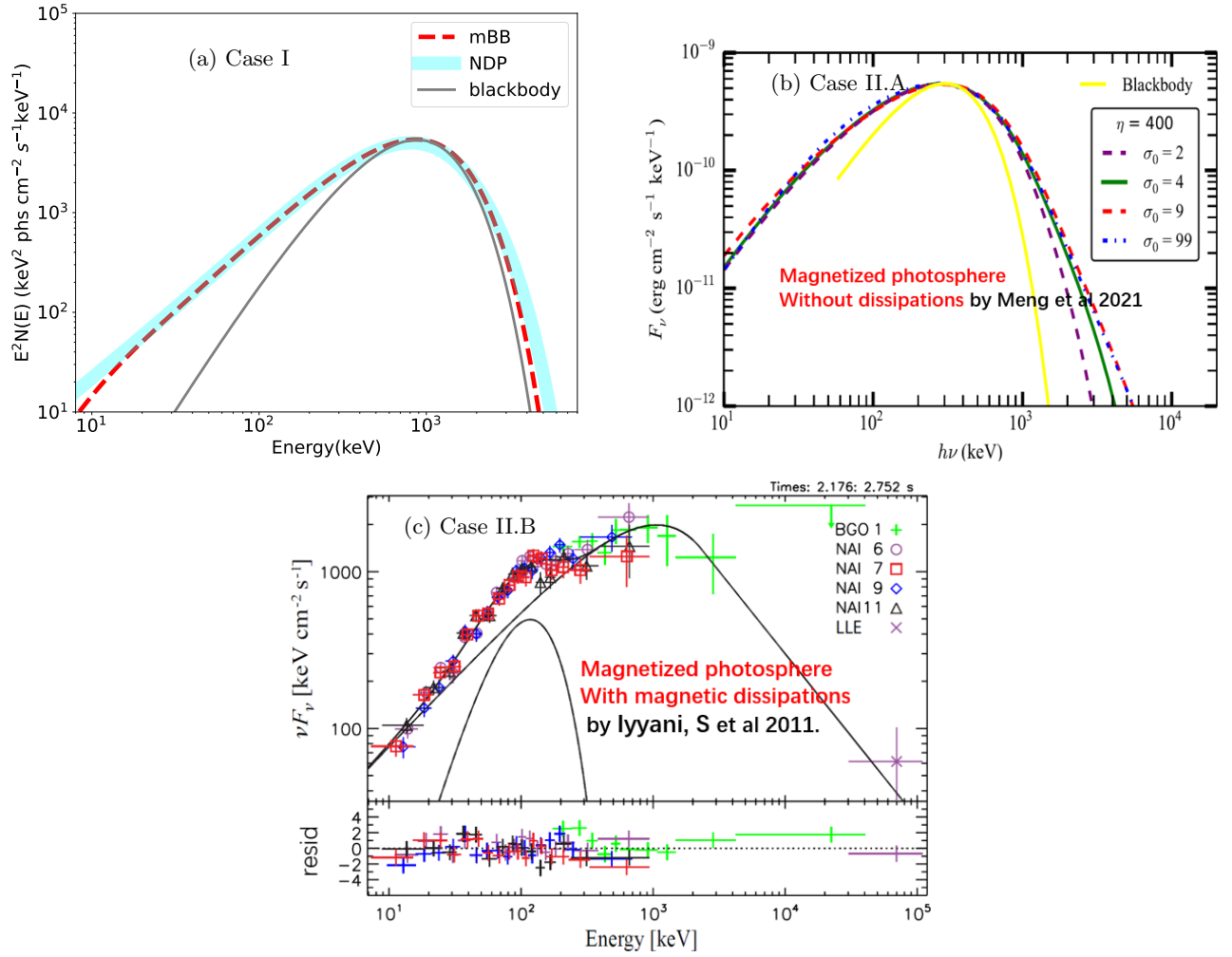


Figure 1. (a) Case I: the spectra of mBB, NDP and BB functions from the pure hot fireball. (b) Case II.A: the F_ν spectra from the magnetized photosphere without dissipations adapted from Figure 7 (a) in Meng et al. (2022) with different magnetization parameters. (c) Case II.B: the spectrum from the magnetized photosphere with magnetic dissipations adapted from Figure 1 in Iyyani et al. (2013).

- **I.** the pure hot fireball with or without dissipations; there is not Poynting flux in the outflow while the matter flux is dominant. From the above discussion, the spectrum of the quasi-thermal (QT) emission may be boarder than a blackbody (BB) function with a single temperature. GRB 210121A is a typical GRB from a pure hot fireball (Wang et al. 2021; Song et al. 2022a) and the spectrum is well consistent with the probability non-dissipative photosphere (NDP) model (Lundman et al. 2013) from a pure hot fireball. In this case, the dimensionless entropy $\eta = L_w/Mc^2$ (\dot{M} is the mass rate of baryon loading; L_w is the wind luminosity) or the Lorentz factor increases with time. As shown in Figure 1 (a), the spectrum of mBB model are similar to that of the NDP model (their parameters are from the fit results to the spectrum of GRB 210121A in the first 0.9 s). They are both broader than that of the BB spectrum (with the temperature $kT = E_p/\zeta$, $\zeta \sim 3$ according to Zhang et al. (2012), and E_p is the peak energy of the νF_ν spectrum). This is mainly due to the geometrical broadening and the jet structure;

- **II. a hybrid outflow in which the matter flux and Poynting flux both exist; in the case, we have $L_w = L_m + L_p$ and**

$$\eta(1 + \sigma_0) = \frac{L_m + L_p}{Mc^2}, \quad (1)$$

where the magnetization factor σ_0 is the ratio of Poynting flux luminosity to the matter flux; L_p is the luminosity of Poynting flux and L_m is the luminosity of matter flux, and $\eta = \frac{L_m}{Mc^2}$. There are three different cases that may occur in a hybrid outflow (Gao & Zhang 2015):

- **II.A** the Poynting flux could accelerate the outflow without any magnetic dissipation; the magnetic energy is only converted into the kinetic energy of the bulk motion. The spectrum could be still QT. However, as shown in Figure 1 (b), they are also broader than the Planck spectrum, which is similar to the cases of pure hot fireball, especially with a low to moderate magnetization, e.g. $\sigma_0 < 10$ (Meng et al. 2022);
- **II.B** the magnetic dissipation could be caused below the photosphere, and produces a spectrum with a non-thermal (NT) appearance with a large E_p (e.g. Beloborodov 2013). GRB 110721A is diagnosed to have a significant magnetic dissipation (Gao & Zhang 2015). As shown in Figure 1 (c), the spectrum of GRB 110721A could be described by a thermal component (denoted with a BB) plus a NT component (denoted by a BAND function) (Iyyani et al. 2013);
- **II.C** the Poynting flux could be thermalized completely below the photosphere due to the existence of the extra thermal component in the outflow. In this case, the spectrum may be similar to the case of I.

For the case of II.B, the shape of νF_ν spectrum could be hump-like¹, in which the thermal component is in the lower energy band while the NT component from the magnetic dissipation has a larger E_p (1 MeV \sim 20 MeV). There are two components evidently in the spectrum in this case. By comparison, the spectrum of Case II.A is similar with that of pure hot fireball in Case I, especially if the outflow has a low to moderate magnetization with a small σ_0 . There seems only one QT component in the spectrum. In this paper, we focus on the cases I and II.A. In these cases, the QT component is dominant in the prompt phase and the spectrum is not hump-like, the combined model of BB+NT may be not the best model to describe the spectrum, which is proved in the following analysis.

Gao & Zhang (2015) proposes a ‘top-down’ approach to diagnose the properties of the magnetization of the central engine. In this approach, these impacts from the jet structure and geometrical broadening on the spectrum shape are not considered, and the spectrum of photospheric emission is taken to be a BB with single temperature. The diagnosis is easy to be performed for the emission with a hump-like spectrum which is well described with BB+NT model where the NT component is denoted by a BAND or a exponential cut-off power law (CPL) function. However, one question is raised: how to diagnose a photospheric emission which may be from the Case II.A or I? This has not been discussed in former works. There may be some problems with BB+CPL/BAND model in the case of QT-dominated emission, **which are proved in the following analysis:** 1) the obtained flux of BB component, F_{BB} , is very small compared to the total flux of thermal component; 2) the low energy photon index α of CPL/BAND function may be still greater than the synchrotron death line (Preece et al. 1998), $-2/3$ (e.g., as shown in Table 2 in Chen et al. 2022), which implies this so-called NT component is also from photospheric emission; and 3) the obtained temperature of BB, $kT \sim 1/3E_p$, and this means that there may be not two kinds of components (thermal and NT) in the emission, thus, the contribution from the photosphere is underestimated substantially. In this paper, we use a characteristic temperature with corresponding flux for the QT-dominated spectrum **to replace the temperature and flux of a BB in BB+NT modeling in the diagnosis of magnetization.** Some control samples are used in order to test the validity of this method. One control sample is GRB 210121A, of which the prompt emission is mainly from a typical pure hot fireball and the spectrum could be described with a mBB or NDP model (Wang et al. 2021; Song et al. 2022a); the other one is GRB 210610B, which is also dominated by the photospheric emission and

¹ in some works (e.g., Giannios 2006), the photospheric emission is enhanced by the magnetic dissipation below the photosphere and could produce a spectrum only with NT appearance.

determined to be from a hybrid outflow (Chen et al. 2022). Note that the diagnosis for magnetization is performed with the fit results with the BB+NT model. However, the spectrum of GRB 210610B is not evidently hump-like. In this analysis, we perform the diagnosis for magnetization by modeling with mBB or mBB+NT model. The validity of our method could be confirmed from the comparison with the former method in the following analysis.

GRB 221022B is recently detected by several missions, such as Fermi/GBM (GCN 32830, Poolakkil et al. 2022), GRBAlpha (GCN 32844, Ohno et al. 2021) konus-wind (GCN 32864, Ridnaia et al. 2022) and *Insight*-HXMT. The prompt emission has a long duration of about 50 s. Its prompt emission behaves a typical evolution from thermal to non-thermal, which is a representative for some bursts. According to the analysis, we find that it is from a hot fireball with an increasing Lorentz Factor at the beginning, which is well consistent with a typical expanding fireball scenario. Note that our method of magnetization diagnosis is also applied to this burst, and the results are consistent well with the theoretical prediction from the photosphere model of a pure hot fireball, so that the validity of our method is still confirmed in GRB 221022B.

The paper is organized as follows: in Section 2, the methods for binning, background estimation, spectral fitting and model selection are introduced; in Section 3, the characteristic temperature for quasi-thermal emission is introduced; some control samples with known properties of the outflow, are used to test this method; in Section 4, the modeling of GRB spectra is introduced; basic data analysis for GRB 221022B is performed; in Section 5, we speculate and discuss the emission mechanism of prompt emission by employing ‘top-down’ approach with the characteristic temperature; the conclusion and summary are given in Section 6.

2. METHODS FOR DATA ANALYSIS

2.1. Binning method of light curves for time-resolved spectra

In this work, the Bayesian blocks (BBlocks) method introduced by Scargle et al. (2013) and suggested by Burgess (2014), is applied with a false alarm probability $p_0 = 0.01$ on light curves. In some cases, the blocks are coarse for fine time-resolved analysis. Burgess (2014) suggested that the constant cadence (CC) method is accurate when the cadence is not too coarse. Therefore, we take a combination of BBlocks and CC methods, fine binning of constant cadence are performed in each block, and only the bins with the signal-to-noise ratio (S/N) ≥ 40 at least in one detector should be utilized.

2.2. Background estimation, spectral fitting method and model selection

A polynomial is applied to fit all the energy channels and then interpolated into the signal interval to yield the background photon count estimate for GRB data. The Markov Chain Monte Carlo (MCMC) fitting is performed to find the parameters with the maximum Poisson likelihood. The best model is determined by the method of bayesian information criterion (BIC, Wei et al. 2016), where BIC is defined as

$$\text{BIC} = -2\ln\mathcal{L} + \ln(N)n, \quad (2)$$

\mathcal{L} denotes the likelihood function for all these parameters based on a Bayesian prior, N is the number of data points, and n is the number of free parameters; ΔBIC is the difference of BIC values of two models. A model that has a lower BIC value than the other is preferred. If the change of BIC between these two models, ΔBIC is from 2 to 6, the preference for the model with the lower BIC is positive; if ΔBIC is from 6 to 10, the preference for that is strong; and if ΔBIC is above 10, the preference is very strong.

3. A GENERALIZED APPROACH FOR MAGNETIZED PHOTOSPHERE FOR QUASI-THERMAL EMISSION

3.1. The characteristic temperature and corresponding flux for quasi-thermal emission

We find many quasi-thermal emission could be described as a mBB function, in which the flux and the temperature of the individual Planck function is related by a power law with index q (Ryde et al. 2010),

$$F(T) = F_{\max}(T/T_{\max})^q, \quad (3)$$

where F_{\max} is the integrated flux of the Planck spectrum with a temperature of T_{\max} . For mBB, the spectrum consists of a superposition of Planck functions in the temperature range from T_{\min} to T_{\max} .

Here we assume that the multi-color superposition is due to the angle dependence of the Doppler shift. Considering the connection between the observed temperature T_{obs} and T'_{ph} in comoving frame,

$$T_{\text{obs}} = D(\theta)T'_{\text{ph}}/(1+z), \quad (4)$$

where $D(\theta) = (\Gamma(1 - \beta \cos \theta))^{-1}$ is the Doppler factor, θ is the angle to the line of sight of the observer; Γ is the Lorentz factor and $\beta = v/c$. For the emission from magnetized photosphere, T'_{ph} is proportional to $R_{\text{ph}}(\theta)^{-1}$, $R_{\text{ph}}(\theta)^{-(2+\delta)/3}$ or $R_{\text{ph}}(\theta)^{-2/3}$ in different regimes (δ is the index of a power-law scaling for acceleration, $\Gamma \propto r^\delta$, $0 < \delta \leq 1/3$) (e.g., Gao & Zhang 2015). With $R_{\text{ph}}(\theta) \propto \frac{1}{\Gamma^2} + \frac{\theta^2}{3}$ (Pe'er 2008), and assuming that baryon loading is not very sensitive to θ within the opening angle, we easily get a direct conclusion that, the observed temperature reaches maximum in the direction of line of sight, which is the physical meaning of T_{max} in the observation with the simplest assumption of on-axis observation. Note that in fact density profiles of the outflow may be angle-dependent, and the emission probability is a function of r with maximum at $r = R_{\text{ph}}$, the case could be more complex. However, T_{max} could be taken as a probe for the outflow. We do not know the exact structure of the outflow or jet, thus, the following analysis is phenomenological and the spectrum is required to be well described with mBB function.

The work in Gao & Zhang (2015) proposes an approach to speculate the properties for the magnetized photosphere, such as for non-dissipative magnetized photosphere (Case II.A), we have

$$(1 + \sigma_0) \propto \left(\frac{kT_{\text{ob, BB}}}{F_{\text{BB}}} \right)^{4/3} L_w r_0^{2/3}, \quad (5)$$

where L_w is the entire luminosity of the outflow. Note that the estimation is based on the thermal component which is described as a single blackbody function, without considering the structure of the outflow. **Here we give a simple derivative of the ‘top-down’ approach by Gao&Zhang and an explanation of its physical origin. The acceleration of a GRB jet may be proceeded with two mechanisms: thermally driven or magnetically driven. The former is relevant for a hot fireball, which proceeds very rapidly; whereas the latter is relevant for a Poynting flux dominated outflow, which proceeds relatively more slowly. For a more complicated hybrid jet system, we make the assumption that acceleration proceeds first thermally and then magnetically (e.g. Mészáros & Rees 1997; Vlahakis & Königl 2003). Since thermal acceleration proceeds linearly, and the early magnetic acceleration below the magneto-sonic point also proceeds rapidly, we approximately assume that the ejecta first gets accelerated with $\Gamma \propto r$ until reaching a more generally defined *rapid acceleration* radius r_{ra} defined by the larger one of the thermal coasting radius and the magneto-sonic point. Even though magnetic acceleration may deviate from the linear law below r_{ra} , the mix with thermal acceleration would make the acceleration law in this phase very close to linear. Beyond r_{ra} , the jet would undergo a relatively slow acceleration with $\Gamma \propto r^\delta$ until reaching a *coasting radius* r_c . if one ignores deceleration and energy loss, the Γ evolution for a hybrid system may be approximated as**

$$\Gamma(r) = \begin{cases} \frac{r}{r_0}, & r_0 < r < r_{\text{ra}}; \\ \Gamma_{\text{ra}} \left(\frac{r}{r_{\text{ra}}} \right)^\delta, & r_{\text{ra}} < r < r_c; \\ \Gamma_c, & r > r_c, \end{cases} \quad (6)$$

Because in the paper, we focus on Case I and II.A, we take the hybrid outflow without magnetic dissipation as a sample. This scenario assumes that no magnetic field reconnection occurs below the photosphere, so that no magnetic energy is directly converted to particle energy and heat. Without magnetic heating, the thermal energy undergoes adiabatic cooling, with $r^2 e^{3/4} = \text{const}$ (e.g. Piran et al. 1993). Noticing $e \propto T'^4$ and the dynamical evolution Equation (6), one can derive the comoving temperature at the photosphere radius r_{ph} as

$$T'_{\text{ph}} = \begin{cases} T_0 \left(\frac{r_{\text{ph}}}{r_0} \right)^{-1}, & r_0 < r_{\text{ph}} < r_{\text{ra}}; \\ T_0 \left(\frac{r_{\text{ra}}}{r_0} \right)^{-1} \left(\frac{r_{\text{ph}}}{r_{\text{ra}}} \right)^{-(2+\delta)/3}, & r_{\text{ra}} < r_{\text{ph}} < r_c; \\ T_0 \left(\frac{r_{\text{ra}}}{r_0} \right)^{-1} \left(\frac{r_c}{r_{\text{ra}}} \right)^{-(2+\delta)/3} \left(\frac{r_{\text{ph}}}{r_c} \right)^{-2/3}, & r_{\text{ph}} > r_c. \end{cases} \quad (7)$$

Here

$$T_0 \simeq \left(\frac{L_w}{4\pi r_0^2 a c (1 + \sigma_0)} \right)^{1/4}, \quad (8)$$

is the temperature at r_0 , $a = 7.56 \times 10^{-15} \text{ erg cm}^{-3} \text{ K}^{-4}$ is radiation density constant. Given the central engine parameters L_w , r_0 , η and σ_0 , we can derive all the relevant photosphere properties with equations from (1), (6) and (7), as long as the slow magnetic acceleration index δ is determined. The largest δ is 1/3, which is achievable for an impulsive, non-dissipative magnetic shell (Granot et al. 2011). For different central engine parameters, Γ_{ra} can have two possible values: η or $[\eta(1 + \sigma_0)]^{1/3}$. For each case, the photosphere radius r_{ph} can be in three different regimes separated by r_{ra} and r_c , thus there are six saturated regimes of rapid acceleration, including **Regime I**: $r_{\text{ph}} < r_{\text{ra}}$ with $\eta > (1 + \sigma_0)^{1/2}$; **Regime II**: $r_{\text{ra}} < r_{\text{ph}} < r_c$ with $\eta > (1 + \sigma_0)^{1/2}$; **Regime III**: $r_{\text{ph}} > r_c$ with $\eta > (1 + \sigma_0)^{1/2}$; **Regime V**: $r_{\text{ra}} < r_{\text{ph}} < r_c$ with $\eta < (1 + \sigma_0)^{1/2}$; **Regime VI**: $r_{\text{ph}} > r_c$ with $\eta < (1 + \sigma_0)^{1/2}$; and **Regime IV**: ($r_{\text{ph}} < r_{\text{ra}}$ with $\eta < (1 + \sigma_0)^{1/2}$). Relevant parameters are derived in each regime, including r_{ra} and r_c , along with the photosphere properties, i.e. r_{ph} , $(1 + \sigma_0)$, kT_{ob} , and F_{BB} accordingly, and more details of the formulae could be found in Appendix A.

Some quasi-thermal spectra might be broader than a BB, and it is more reasonable that their spectra are described with a mBB function rather than a BB function with a single temperature. Thus, we should use the parameters obtained from modeling with mBB to estimate the properties of photospheric emission. In some works, BB plus an empirical functions (such as CPL, BAND²) is used, in order to estimate the observed temperature ($kT_{\text{ob, BB}}$) and flux of thermal component (F_{BB}). However, from above discussion in the introduction, we think this method is not good enough, because the extracted values of F_{BB} are always very small compared with those of total flux if it is a quasi-thermal-dominated emission. From Equation (5), $(1 + \sigma_0)$ may be overestimated; besides, because of the underestimated F_{BB} , the possible ranges of r_0 are broad, so that the regimes can not be well determined. In this case, $(1 + \sigma_0)$ could vary from ~ 1 to several tens with different orders of r_0 , which is not convincible.

Therefore, we should consider a better approach for these cases. Considering the derivative of flux of mBB function has form of

$$\frac{dF(T)}{dT} = q \frac{F_{\text{max}}}{T_{\text{max}}^q} T^{q-1}, \quad (9)$$

integrating Equation (9) to get a bolometric integrated spectral flux F_{mBB} , we have

$$F_{\text{max}} = F_{\text{mBB}} / \left(1 - \left(\frac{kT_{\text{min}}}{kT_{\text{max}}} \right)^q \right). \quad (10)$$

$F_{\text{max}} \gtrsim F_{\text{mBB}}$ when $q > 0$ and $kT_{\text{min}} \ll kT_{\text{max}}$. In some works (e.g., Hou et al. 2018), other form of derivative of mBB function is used as

$$\frac{dF(T)}{dT} = \frac{m+1}{\left(\frac{T_{\text{max}}}{T_{\text{min}}} \right)^{m+1} - 1} \frac{F_{\text{mBB}}}{T_{\text{min}}} \left(\frac{T}{T_{\text{min}}} \right)^m, \quad (11)$$

where m is the index of the distribution of dF/dT , thus we have $q = m + 1$.

In summary, we use $kT_{\text{max}} - F_{\text{max}}$ as the characteristic temperature and the corresponding flux for the quasi-thermal emission, to replace $kT_{\text{ob, BB}} - F_{\text{BB}}$ in diagnosing the magnetization of the outflow. If we do not consider the intermediate photosphere (see Song & Meng 2022, for similar details) in the outflow, $kT_{\text{max}} - F_{\text{max}}$ could be taken as a good probe for the properties of the outflow. If $(1 + \sigma_0) > 1$, QT emissions are from magnetized photosphere. σ_{15} determined at radius $r = 10^{15} \text{ cm}$ is used to speculate the origin of NT emissions if it exists in the emission. Note that we do not know the initial radius r_0 for the outflow, thus we first assume a series of $r_0 = 10^7 - 10^9 \text{ cm}$ in the calculation, however, it is found that only a narrow range of r_0 could give reasonable results with constraints from η , $(1 + \sigma_0)$, r_{ra} , r_{ph} , and r_c for each regime. **We consider these saturated regimes of rapid acceleration, including Regime II, III, V and VI. For the unsaturated regimes, such as Regimes I and IV, η can not be determined from the observation, which are not considered. Besides, the typical value, $Y = 2$, is considered in the procedure, where Y is the ratio between the total fireball energy and the energy**

² The formulae for spectral models are described in Appendix B.

Table 1. The time-resolved results of GRB 210610B with mBB (+NT).

Time bins (s)	m	kT_{\min} (keV)	kT_{\max} (keV)	F_T (10^{-6} erg cm $^{-2}$ s $^{-1}$)	α	F_{NT} (10^{-6} erg cm $^{-2}$ s $^{-1}$)	BIC	$\frac{\chi^2}{ndof}$	r_0 ($\times 10^8$ cm) Regime II	r_0 ($\times 10^8$ cm) Regime III
[-10, 25]	$0.80^{+0.10}_{-0.20}$	$1.7^{+3.8}_{-1.0}$	$133.0^{+31.3}_{-36.7}$	$0.30^{+0.07}_{-0.10}$	$-1.72^{+0.32}_{-0.31}$	$0.16^{+0.03}_{-0.06}$	179.6	$\frac{166.2}{166}$	[0.5, 1.6]	[0.1, 0.3]
[25, 35]	$0.26^{+0.04}_{-0.08}$	$9.1^{+1.8}_{-1.8}$	$176.0^{+8.7}_{-7.8}$	$5.37^{+0.13}_{-0.13}$	$-2.66^{+0.39}_{-0.22}$	$0.23^{+0.07}_{-0.06}$	171.5	$\frac{158.1}{166}$	[1.7, 3.9]	[0.3, 0.6]
[35, 45]	$0.29^{+0.03}_{-0.05}$	$3.1^{+1.2}_{-1.1}$	$125.6^{+8.0}_{-5.5}$	$2.81^{+0.09}_{-0.07}$			159.9	$\frac{150.9}{168}$	[2.4, 5.5]	[0.4, 0.8]
[45, 55]	$-0.46^{+0.32}_{-0.27}$	$9.6^{+1.9}_{-1.7}$	$102.9^{+22.3}_{-33.5}$	$1.13^{+0.07}_{-0.09}$	$-2.56^{+0.14}_{-0.56}$	$0.25^{+0.05}_{-0.09}$	155.6	$\frac{142.2}{166}$	[3.0, 6.1]	[0.5, 0.9]
[55, 100]	$-0.23^{+0.25}_{-0.27}$	$3.7^{+1.6}_{-1.3}$	$45.7^{+5.8}_{-6.5}$	$0.19^{+0.02}_{-0.01}$	$-2.53^{+0.05}_{-0.32}$	$0.10^{+0.01}_{-0.03}$	238.1	$\frac{224.7}{166}$	[4.0, 11.6]	[0.5, 1.1]

emitted, and $Y \gtrsim 1$. Constant or decreasing r_0 values with time are both accepted, if one considers the depletion of the envelope.

If $(1 + \sigma_0) \simeq 1$, it is similar to the case of the pure hot fireball (Case I). In this case, r_0 could be directly determined by the method in Pe'er et al. (2007). The generalized method with $kT_{\max} - F_{\max}$ can be applied in this case as well.

3.2. Test with control samples: GRB 210121A and GRB 210610B

3.2.1. A control sample of Case II.A: GRB 210610B

For comparison, GRB 210610B originated from a hybrid jet (Chen et al. 2022), is also used to test this method, and $(1 + \sigma_0) > 1$ is expected at least in one time bin in time-resolved analysis.

We divide the prompt phase into five time intervals: [-10, 25] s, [25, 35] s, [35, 45] s, [45, 55] s and [55, 110] s relative to T_0 (T_0 is the trigger time of the corresponding GRB, the same below). The preferred model for the spectrum in [35, 45] s is mBB while the other time-resolved spectra are best described by a combined model of mBB+PL. The fit results with the best models are shown in Table 1. We take the spectrum in $T_0 + [25, 35]$ s which has the highest flux for example, to show the modeling selection between BB+BAND and mBB+PL. As shown in Figure 2 (a)-(d), the spectrum is not hump-like. If modeling with a CPL function, one has $\alpha = -0.37 \pm 0.02$ and $E_p = 379.5 \pm 3.5$ keV. The extracted parameters and BIC values for these two combined models are listed as below:

- **BB+BAND:** for BB, $kT = 135.3 \pm 14.1$ keV and flux $F_{\text{BB}} = (2.81 \pm 0.04) \times 10^{-6}$ erg cm $^{-2}$ s $^{-1}$; for BAND: $\alpha = -0.35 \pm 0.02$, $\beta = -9.37 \pm 0.72$, $E_p = 224.5 \pm 10.6$ keV and $F_{\text{BAND}} = 2.63 \pm 0.27$ erg cm $^{-2}$ s $^{-1}$. BIC=179.9 with a freedom degree of 166;
- **mBB+PL:** for mBB, $m = 0.26 \pm 0.06$, $kT_{\min} = 9.1 \pm 1.1$ keV, $kT_{\max} = 176.0^{+8.7}_{-7.8}$ keV, $F_{\text{mBB}} = (5.37 \pm 0.13) \times 10^{-6}$ erg cm $^{-2}$, s $^{-1}$; for PL: $\alpha = -2.66^{+0.39}_{-0.22}$, $F_{\text{PL}} = 0.23 \pm 0.06$ erg cm $^{-2}$ s $^{-1}$. BIC=171.5 with a freedom degree of 166.

These two models both describe the spectrum well, however, from the aspect of BIC values, mBB model is preferred with $\Delta\text{BIC} = 8.4$. Besides, there are some features of extracted parameters of BB+BAND which could not be ignored: 1) $\alpha \sim -0.35$ is well above -2/3 for the BAND component in BB+BAND, which may be difficult to be interpreted as a NT emission; for comparison, $\alpha \sim -1$ in the BAND component in GRB 110721A (Iyyani et al. 2013); 2) $kT = 135.3 \pm 14.1$ keV for BB components corresponds to a peak energy of $3kT \sim 400$ keV, which is consistent with E_p of the whole spectrum. Considering that the component described with BAND is also QT, we inferred that the QT component is dominant. Therefore, mBB+PL is better from both of the physical meaning and model selection.

The possible values of r_0 are estimated with the method in Section 3 are listed in the last two columns in Table 1. A narrow range ($0.5 \times 10^8 - 0.6 \times 10^8$ cm) is obtained with assuming that r_0 could be taken as a constant during the prompt phase. The possible regime for $T_0 + [-10, 25]$ s is II, while Regime III is reasonable for the other part of prompt phase. The estimated $(1 + \sigma_0)$ is greater than 1 for most bins as shown in Figure 2 (e). σ_0 ranges from 0 to

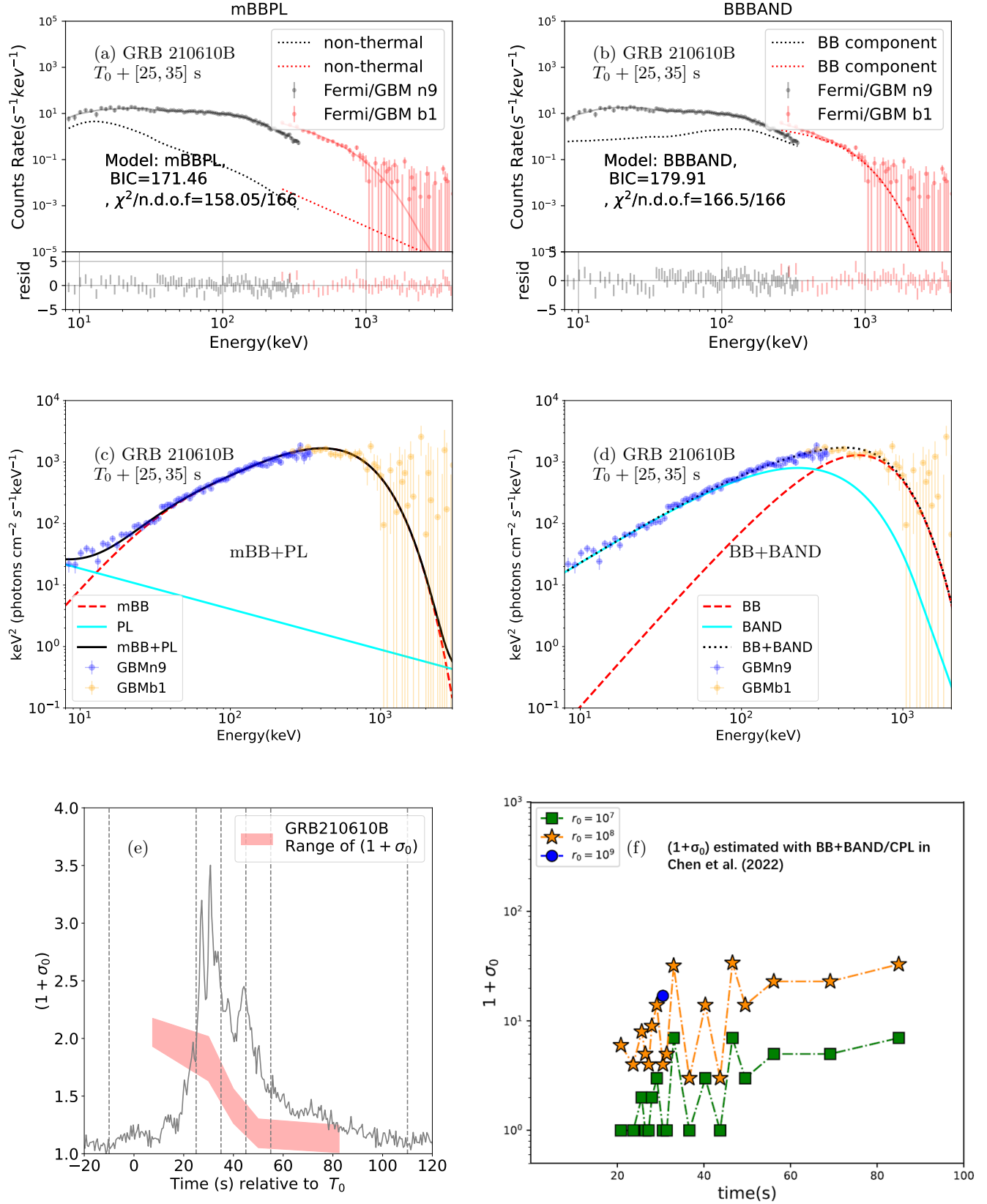


Figure 2. (a) and (b) are spectra and fit results with mBB+PL and BB+BAND models, while the corresponding panels below, (c) and (d) are model shapes in the $E^2 N(E)$ form. (e) $1 + \sigma_0$ estimated from modeling with mBB (+NT). **The gay line denotes shape of the normalized light curve, the same below. The vertical dashed lines denote the time internals.** (f) $1 + \sigma_0$ estimated from modeling with BB+NT, adapted from Figure 3 (b) in Chen et al. (2022).

Table 2. The time-resolved results of GRB 210121A with the mBB.

Time bins	m	kT_{\min}	kT_{\max}	F_T	BIC	$\frac{\chi^2}{ndof}$	r_0 ($\times 10^8$ cm) ^a	r_0 ($\times 10^7$ cm)
(s)		(keV)	(keV)	(10^{-6} erg cm $^{-2}$ s $^{-1}$)			Regime II	Regime III
[-0.01, 2.19]	$0.54^{+0.05}_{-0.05}$	$3.0^{+2.5}_{-1.5}$	$397.0^{+28.7}_{-23.5}$	$16.46^{+0.91}_{-0.71}$	206.4	$\frac{197.3}{192}$	[0.4, 0.8]	[0.3, 2.3]
[2.8, 14.9]	$0.33^{+0.05}_{-0.04}$	$1.8^{+0.9}_{-0.6}$	$356.5^{+39.8}_{-28.1}$	$4.75^{+0.31}_{-0.28}$	202.8	$\frac{193.6}{192}$	[0.2, 0.5]	[0.1, 1.1]

^aHere the ranges of r_0 are given with $Y = 2$. Considering that GRB 210121A is from a pure hot fireball in fact and $Y = 1$, the possible ranges of r_0 are $[0.6, 0.8] \times 10^8$ cm, $[0.4, 0.5] \times 10^8$ cm for two time intervals in Regimes II, and $[0.4, 0.7] \times 10^8$ cm, $[0.1, 0.3] \times 10^8$ cm in Regime III.

1.2, which means a low to moderate magnetization in the outflow. The estimated σ at $r = 10^{14}$ to 10^{15} cm is less than 1, which corresponds to a coasting regime at these radii, and the NT emission is mainly from IS mechanism. This is consistent with the conclusion of [Chen et al. \(2022\)](#). However, $1 + \sigma_0$ is constrained to a much narrower range with our method, while it ranges from 1 to several tens with BB+BAND modeling in [Chen et al. \(2022\)](#). **Besides, there is another evidence that mBB+PL provides a much more reasonable physical explanation than that by BB+BAND: we note that the BAND component has a large flux which reaches up to nearly a half contribution in BB+BAND; however, IS mechanism has a much lower radiative efficiency (only a few percent, [Zhang & Yan 2011](#)), thus it is not reasonable that this large component denoted by a BAND function is the NT emission produced from the IS mechanism. For mBB+PL model, the NT emission is denoted by a PL with a much smaller flux, which provides more reasonable explanation.**

Figure 2 (f) shows $(1 + \sigma_0)$ estimated with BB+BAND model and different r_0 values of 10^7 cm, 10^8 cm and 10^9 cm in [Chen et al. \(2022\)](#). We can see that σ_0 varies from a few to tens. In fact, if $\sigma_0 = \frac{L_p}{L_m} > 10$, the outflow is dominated by the Poynting flux, so that the spectrum likely has a NT appearance as that in e.g. GRB 211211A with σ_0 of tens to a hundred ([Chang et al. 2023](#)). However, the photospheric emission in GRB 210610B is evident and dominant in most time bins, a very large σ_0 may not be reasonable. Note that according to the Equation (5), F_{BB} in the denominator is smaller than the truth, which might cause an overestimation for σ_0 . This accounts for the large σ_0 obtained with BB+BAND model. In our method, $(1 + \sigma_0)$ is constrained to a more reasonable value of a few.

3.2.2. A control sample of Case I: GRB 210121A from a pure hot fireball

As discussed in [Wang et al. \(2021\)](#) and [Song et al. \(2022b\)](#), the prompt emission of GRB 210121A is mainly from a pure hot fireball. The spectra in both epochs ($[T_0 - 0.01, T_0 + 2.19]$ s and $[T_0 + 2.8, T_0 + 14.8]$ s, T_0 is the trigger time of the corresponding GRB, the same below) are well described with a NDP model of a pure hot fireball. **If the method discussed in this analysis does work, $(1 + \sigma_0) \simeq 1$ should be accepted for both epochs.**

Here we take $[T_0 - 0.01, T_0 + 2.19]$ s with the highest flux for example to compare the difference between modeling with mBB and BB+BAND models. The fit results and spectra are shown in [Figure 3 \(a\)-\(d\)](#), and parameters are listed as below,

- **BB+BAND:** for BB, $kT = 300.3 \pm 25.1$ keV and $F_{BB} = (11.07 \pm 0.14) \times 10^{-6}$ erg cm $^{-2}$ s $^{-1}$; for BAND: $\alpha = -0.32 \pm 0.04$, $\beta = -9.92 \pm 0.92$, $E_p = 224.5 \pm 10.6$ keV and $F_{BAND} = 6.06 \pm 0.19$ erg cm $^{-2}$ s $^{-1}$. BIC=217.2 with a freedom degree of 190;
- **mBB:** for mBB, $m = 0.54 \pm 0.05$, $kT_{\min} = 3.04^{+2.5}_{-1.5}$ keV, $kT_{\max} = 397.0^{+28.7}_{-23.5}$ keV, $F_{mBB} = (16.46^{+0.91}_{-0.71}) \times 10^{-6}$ erg cm $^{-2}$, s $^{-1}$; BIC=197.3 with a freedom degree of 192.

It seems that the case is similar to that in GRB 210610A, mBB is still preferred in GRB 210121A. [Figure 3 \(e\) and \(f\)](#) show the estimated $(1 + \sigma_0)$ for GRB 210121A with mBB model. For GRB 210121A, spectra are well described with a mBB model for both epochs, and the fit results are listed in [Table 2](#).

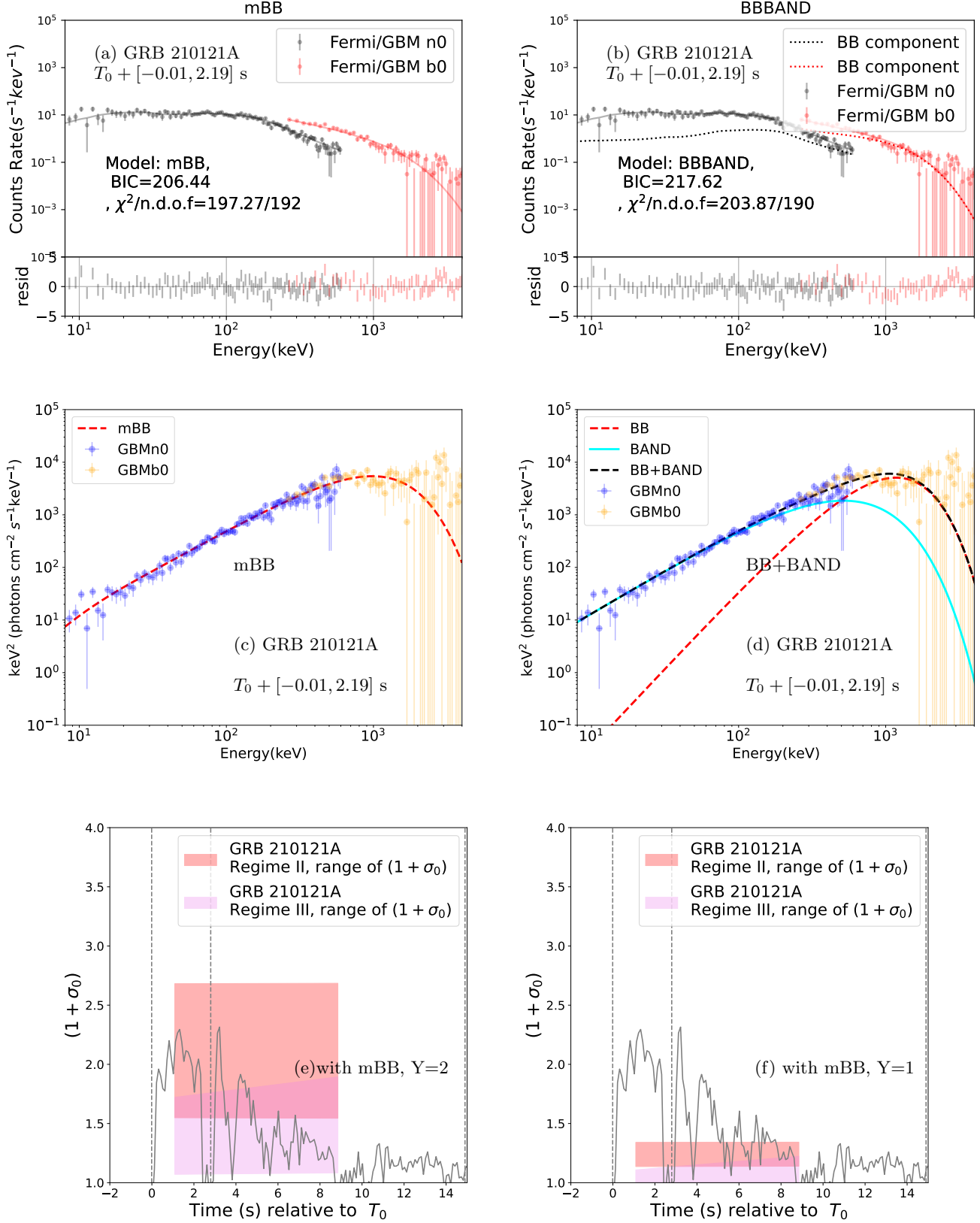


Figure 3. (a)-(b) are the spectra and fit results with mBB and BB+BAND models and BIC values while the corresponding panels below, (c) and (d) are model shapes in the $E^2 N(E)$ form. (e) and (f): The ranges of $(1 + \sigma_0)$ for GRB 210121A with $Y = 1$ and $Y = 2$. Note that they are both estimated with the fit results from mBB modeling.

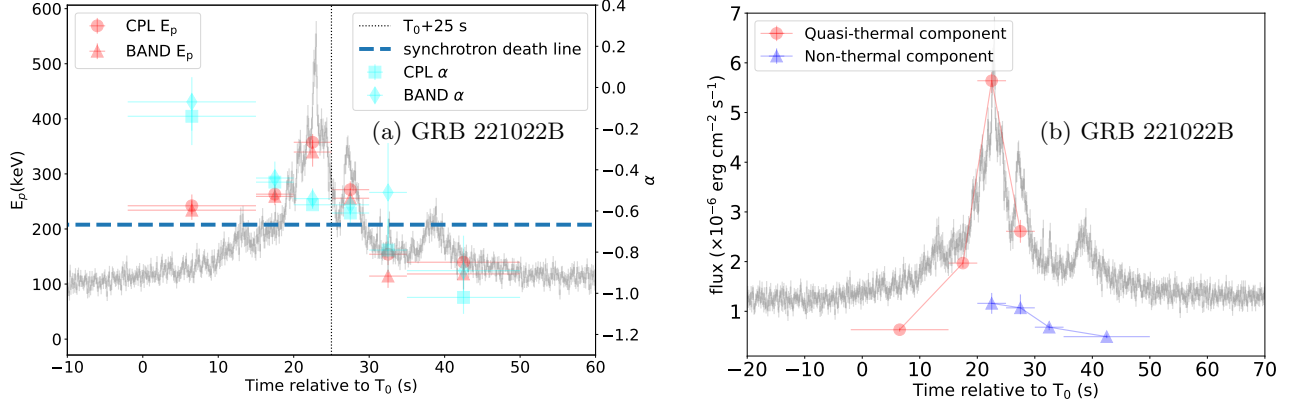


Figure 4. (a) The evolution of α and E_p of GRB 221022B. (b) The flux of QT and NT components of GRB 221022B.

More details about the modeling parameters could be found in the published works (e.g. Wang et al. 2021; Song et al. 2022b), thus we do not show them again in this analysis.

We find both of two regimes (II and III) are possible. The possible r_0 ranges are listed in Table 2. Though $1 + \sigma_0$ could be greater than 1 in Regime II, $\sigma_0 < 0.1$ and $1 + \sigma_0 \simeq 1$ is not ruled out for both epochs because Regime III could work as well. Note that in the case of pure hot fireball, the radiative efficiency is very high, so that Y may be smaller than 2. $\sigma_0 \simeq 1$ with $Y = 1$ could work in Regime II as well as shown in Figure 2 (b). Therefore, for the quasi-thermal-dominated GRBs with unknown properties, we could perform a similar procedure to test if $1 + \sigma_0 \simeq 1$ could be ruled out with $Y = 2$.

3.3. The Validity of the method

From analyses of the control samples, a summary is obtained from the comparison between our method (mBB or mBB+NT: $kT_{\max} - F_{\max}$) and the former one (BB+NT: $kT_{\text{BB}} - F_{\text{BB}}$):

- **modeling:** our method (mBB or mBB+NT: $kT_{\max} - F_{\max}$) could be preferred if the quasi-thermal spectrum is not hump-like;
- **the estimation for r_0 and σ_0 :** the estimated range of r_0 with our method (mBB or mBB+NT: $kT_{\max} - F_{\max}$) is narrower compared with those ranging from 10^7 cm to 10^9 cm. For the case of pure hot fireball (Case I), $1 + \sigma_0 \simeq 1$ is not ruled out, and this is robust for different Y values. For the hybrid outflow (Case II.A), $1 + \sigma_0 > 1$ could be obtained; compared with the results of the former method, the estimated parameters with our method are more reasonable.

4. BASIC ANALYSIS OF GRB 221022B

GRB 221022B is a long burst with duration of ~ 50 s. The light curves from Fermi-GBM and HXMT are shown in Figure 4. The data are from one brightest NaI detector (NaI 4) and one brightest BGO detector (BGO 0) of Fermi/GBM. We check the data from $[T_0 - 300, T_0 + 300]$ s in different energy bands and find that there exists no peaking or bump structure in the background. Fittings with BAND, CPL and mBB are performed on the time-integrated spectrum from $T_0 - 2$ s to $T_0 + 50$ s which contains 95% photons. E_p and bolometric flux in $[T_0 - 2, T_0 + 50]$ s are determined to be $274.41_{-10.69}^{+14.96}$ keV and $1.55_{-0.05}^{+0.03} \times 10^{-6}$ erg cm $^{-2}$ s $^{-1}$ with BAND function. Amati-relation and observed long GRBs with known redshift (e.g., Zhang et al. 2018) give a measurement of $E_p - E_{\text{iso}}$ correlation as $\log E_p(1+z) = (2.22 \pm 0.03) + (0.47 \pm 0.03)\log(E_{\text{iso},\gamma}/10^{52})$. The clustering of long bursts gives a broad range of $z = 0.61_{-0.23}^{+1.49}$ for this burst, and in the following analysis we take $z = 0.61$.

Constant cadence (CC, Burgess 2014) method and Bayesian blocks (BBlocks, Scargle et al. 2013) method with a false alarm probability $p_0 = 0.01$ are used for binning in time-resolved analysis. We also require the signal-to-noise ratio (S/N) ≥ 40 at least in one detector, so we combine some adjacent bins in the beginning and end of the burst. The time bins are [-2, 15] s, [15, 20] s, [20, 25] s, [25, 30] s, [30, 35] s and [35, 50] s relative to T_0 .

The fit results with BAND, CPL, mBB and mBB+PL functions are listed in Table. 3. Spectra of all the time bins could be described well with empirical models (Band and CPL) as well as mBB models. The evolution of α and E_p values are shown in Figure. 4 (a). α decreases with time generally, while E_p tracks the flux roughly. For the first four bins from $T_0 - 2$ s to 30 s it is well above the death line of synchrotron, while after $T_0 + 30$ s, it gradually drops to -1, a typical value for GRBs.

To confirm that the emission is dominated by quasi-thermal component, the combined model of BB+ BAND is used in the modeling. **We find in the first 30 s, $\alpha \sim -0.4$ is obtained for the component described with BAND function, greater than the synchrotron death line. To prove this, we take the spectrum in $T_0 + [-2, 20]$ s as an example. Figure 5 shows the time-integrated spectrum of $T_0 + [-2, 20]$ s and fit results with BB+BAND and mBB. The fit results are listed as below,**

- **BB+BAND: for BB, $kT = 36.3 \pm 12.0$ keV and flux $F_{\text{BB}} = (0.10 \pm 0.04) \times 10^{-6}$ erg cm $^{-2}$ s $^{-1}$; for BAND: $\alpha = -0.35 \pm 0.05$, $\beta = -9.68 \pm 0.72$, $E_p = 280.9 \pm 10.6$ keV and $F_{\text{BAND}} = 0.87 \pm 0.07$ erg cm $^{-2}$ s $^{-1}$. BIC=138.3 with a freedom degree of 120;**
- **mBB: for mBB, $m = 0.49^{+0.13}_{-0.23}$, $kT_{\text{min}} = 5.5^{+3.1}_{-2.4}$ keV, $kT_{\text{max}} = 105.0^{+14.3}_{-7.9}$ keV, $F_{\text{mBB}} = 0.94^{+0.06}_{-0.04} \times 10^{-6}$ erg cm $^{-2}$ s $^{-1}$; BIC=138.0 with a freedom degree of 122.**

The modeling with BB+BAND seems also well, however, it is not better than that with mBB by comparing these two BIC values. mBB is more preferred with a larger freedom degree. Moreover, α of BAND in BB+BAND ~ -0.4 , still well above $-2/3$. Thus the case is similar to that in GRB 210610B as discussed in Section 3.2.1. Moreover, F_{BB} in BB+BAND model is very small compared with the total flux. In the following 20 s, the BB component is very small compared with BAND component which has typical $\alpha = -1$ below the synchrotron death line. The fit quality is not better than those with empirical models as well, so we do not show the fit results here.

An extra component denoted by a PL function is added on the mBB model, to see if there exists non-thermal contribution in the QT-dominated emission. However, for the first and second bins (from $T_0 - 2$ s to 20 s), and the last two bins (from $T_0 + 30$ s to 50 s), the fit quality are not better with combined model of mBB +PL, or the fit results are not reasonable (e.g., $m < -1$). For the former time bins with large α , it may be because there is not evident contribution from extra non-thermal (NT) emission; for the latter with much smaller $\alpha < -2/3$, it is dominated by the NT emission. Around the peak flux from $T_0 + 20$ s to 30 s, we find that the fit results with an extra PL component are better than that only with mBB, especially in $T_0 + 25$ s to 30 s with $\Delta\text{BIC}=7.9$ compared with that only with mBB model. Thus, it seems that in general, evolution from quasi-thermal emission to non-thermal emission occurs during the burst, as shown in Figure 4 (b). It is necessary to extract the magnetization parameters of the outflow and central engine, including $(1 + \sigma_0)$ and $(1 + \sigma_{15})$ at $r = 10^{15}$ cm as the radius for non-thermal emission.

5. THE OUTFLOW PROPERTIES OF GRB 221022B

Some possible origins for the prompt emission of GRB 221022B are listed as below (here we use the notations in the introduction),

- I. QT emissions are from pure hot fireball with or without dissipations; the non-thermal emission is from IS mechanism. In this case, the dimensionless entropy $\eta = L_w/\dot{M}c^2$ or the Lorentz factor increases with time. Note that the radiative efficiency of IS mechanism is low, compared with others for non-thermal (NT) emissions, such as internal-collision-induced magnetic reconnection and turbulence (ICMART, Zhang & Yan 2011).
- II.A QT emissions are from magnetized photosphere without dissipations. The outflow is hybrid, and the Poynting flux is used to accelerate the outflow, rather than thermalized; If the estimated $(1 + \sigma_0) \simeq 1$, we think the matter flux is dominated, and it should go back to case A.
- II.B QT emissions are from magnetized photosphere with dissipations.

Some works (e.g., Giannios 2006; Beloborodov 2013) have predicted a higher E_p varying from 1 MeV up to a maximum value of about 20 MeV in the photosphere due to magnetic dissipation, which is much larger than that

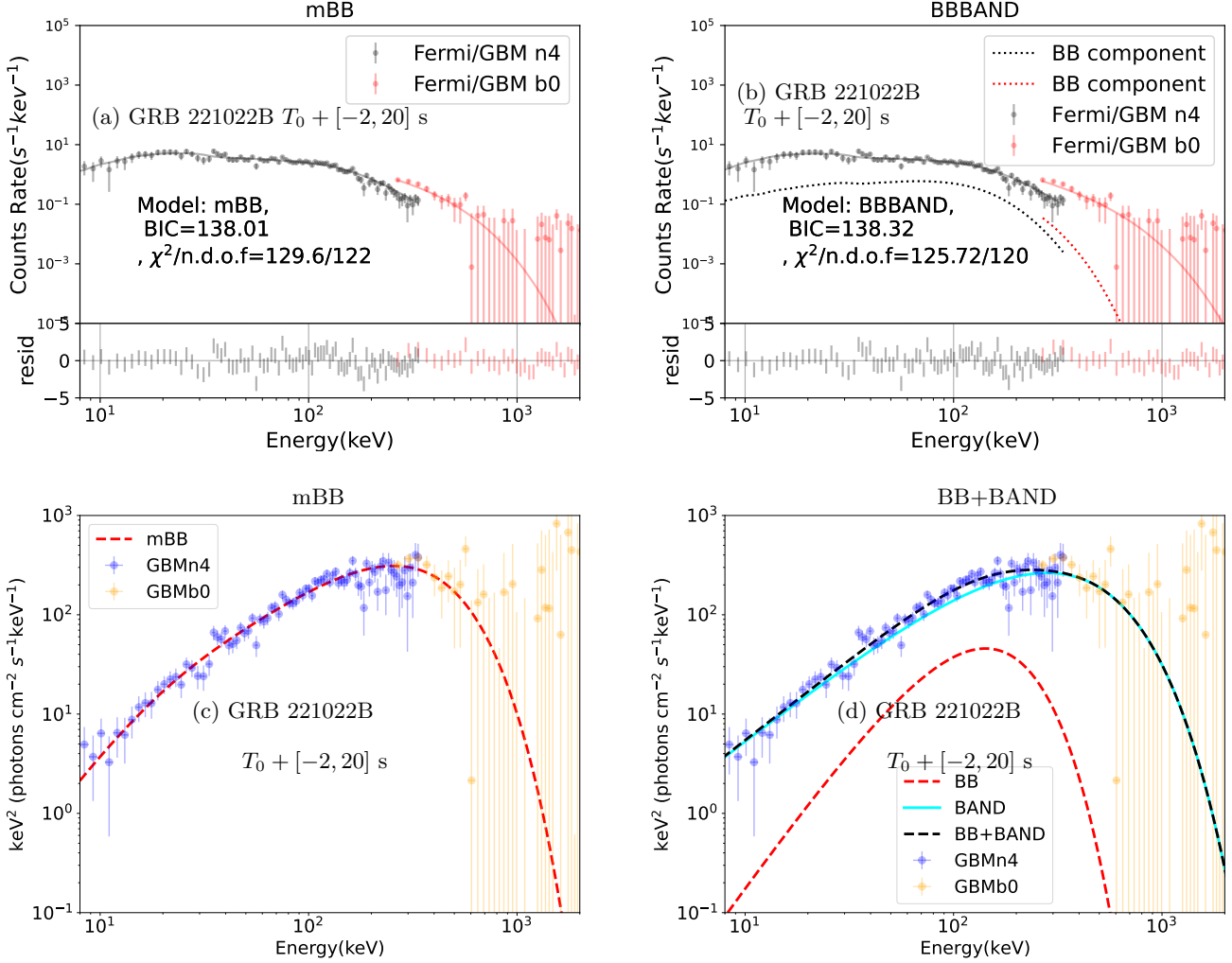


Figure 5. (a)-(b) Spectra of $T_0 + [-2, 20]$ s in GRB 221022B and fit results of BB+BAND and mBB models, (c) and (d) are model shapes in the $E^2 N(E)$ form.

in GRB 221022B. It seems that dissipative magnetic photospheric emission can not interpret the observation of this burst, thus the assumption of II.B is excluded first.

With the method discussed in Section 3, the diagnosis for magnetization is performed, and the possible regimes are II and III. Figure 6 (a)-(d) shows ranges of r_0 , $(1 + \sigma_0)$, η , Γ_{ph} (the Lorentz factor at r_{ph}). In Figure 6 (a), blue and green shadows denote the possible values of r_0 in the Regimes II and III, where r_0 ranges round 10^8 cm, while there exists no reasonable r_0 values from $10^6 - 10^{10}$ cm to satisfy Regimes V and VI. The first two bins ($T_0 - 2$ s to 20 s) could share more or less the same r_0 range, and it seems that r_0 decreases slightly with time in the following two bins ($T_0 + 20$ s to 30 s), which could be acceptable in a collapsar scenario. $(1 + \sigma_0) \simeq 1$ could be accepted in Regime III in the $T_0 + [-2, 30]$ s, which is similar to the that in GRB 210121A. Moreover, $(1 + \sigma_0)$ is also estimated to be less than 1, corresponding to a coasting regime at $r = 10^{14} - 10^{15}$ cm, which implies that in the first 30 s, the small NT is likely from IS mechanism, rather than from ICMART mechanism. Γ_{ph} and η increase with time as shown in Figure 6 (c) and (d), which could also support the conclusion that small NT emission is from IS mechanism during the first 30 s. Therefore, we infer that the photospheric emission in GRB 221022B is mainly from the fireball (Case I).

Besides, there are other evidences for the origin of fireball. The mBB+PL model is not preferred in the beginning of the prompt phase, thus, there exists no dissipation from IS mechanism at early time, at least in the first bin, $T_0 + [-2, 15]$ s. If the outflow is dominated by hot component without dissipation, the spectra should be described well

Table 3. The time-integrated and time-resolved results of GRB 221022B.

Time bins	m	kT_{\min}	kT_{\max}	F_T	α	β	E_p	F_{NT}	BIC	$\frac{\chi^2}{ndof}$
(s)	(keV)	(keV)	(keV)	(10^{-6} erg cm $^{-2}$ s $^{-1}$)				(10^{-6} erg cm $^{-2}$ s $^{-1}$)		
[-2,50]					$-0.63^{+0.03}_{-0.03}$	$-3.47^{+4.03}_{-0.72}$	$274.4^{+15.0}_{-10.7}$	$1.55^{+0.03}_{-0.05}$	251.9	$\frac{242.3}{242}$
	$0.06^{+0.03}_{-0.03}$	$4.2^{+0.5}_{-0.5}$	$131.8^{+9.3}_{-5.2}$	$1.42^{+0.03}_{-0.03}$	$-0.66^{+0.02}_{-0.02}$		$281.8^{+9.0}_{-9.0}$	$1.45^{+0.02}_{-0.04}$	272.3	$\frac{265.2}{243}$
	$-0.13^{+0.08}_{-0.08}$	$12.4^{+5.9}_{-6.5}$	$170.5^{+140.0}_{-37.6}$	$1.31^{+0.05}_{-0.10}$	$-1.69^{+0.07}_{-0.26}$			$0.66^{+0.16}_{-0.55}$	264.7	$\frac{255.2}{242}$
									327.2	$\frac{312.9}{240}$
[-2,15]					$-0.07^{+0.14}_{-0.12}$	$-6.51^{+2.00}_{-5.10}$	$234.1^{+17.5}_{-17.5}$	$0.63^{+0.04}_{-0.04}$	74.4	$\frac{66.0}{122}$
	$0.62^{+0.18}_{-0.18}$	$5.6^{+11.4}_{-3.3}$	$98.1^{+10.0}_{-13.0}$	$0.63^{+0.04}_{-0.04}$	$-0.14^{+0.14}_{-0.11}$		$242.2^{+15.4}_{-20.5}$	$0.63^{+0.05}_{-0.04}$	72.4	$\frac{66.1}{123}$
	$-1.65^{+0.33}_{-0.35}$	$27.7^{+2.0}_{-2.0}$	$1840.1^{+50.6}_{-101.3}$	$0.66^{+0.05}_{-0.13}$	$-1.78^{+0.11}_{-0.36}$			$0.23^{+0.04}_{-0.08}$	75.6	$\frac{67.2}{122}$
									86.9	$\frac{74.3}{120}$
[15,20]					$-0.44^{+0.05}_{-0.08}$	$-6.65^{+2.40}_{-2.20}$	$259.2^{+16.0}_{-16.0}$	$2.03^{+0.08}_{-0.10}$	116.1	$\frac{107.7}{122}$
	$0.31^{+0.08}_{-0.10}$	$3.4^{+2.0}_{-1.8}$	$112.0^{+10.4}_{-12.4}$	$1.97^{+0.09}_{-0.07}$	$-0.46^{+0.08}_{-0.06}$		$263.2^{+14.1}_{-17.6}$	$2.02^{+0.08}_{-0.11}$	113.8	$\frac{107.5}{123}$
	$-0.35^{+1.89}_{-0.12}$	$16.8^{+18.4}_{-9.8}$	$151.6^{+140.0}_{-39.9}$	$1.90^{+0.11}_{-0.08}$	$-1.82^{+0.19}_{-0.11}$			$0.66^{+0.09}_{-0.09}$	118.1	$\frac{109.7}{122}$
									128.7	$\frac{116.1}{120}$
[20,25]					$-0.54^{+0.03}_{-0.05}$	$-2.97^{+0.30}_{-0.10}$	$339.7^{+26.5}_{-22.1}$	$6.64^{+0.17}_{-1.25}$	156.9	$\frac{148.5}{122}$
	$0.10^{+0.05}_{-0.05}$	$5.6^{+0.8}_{-0.8}$	$170.5^{+10.5}_{-9.3}$	$5.83^{+0.15}_{-0.15}$	$-0.57^{+0.02}_{-0.03}$		$357.4^{+11.3}_{-15.1}$	$5.88^{+0.16}_{-0.11}$	164.4	$\frac{158.1}{123}$
	$-0.11^{+0.08}_{-0.13}$	$11.9^{+1.9}_{-1.8}$	$199.5^{+21.7}_{-15.8}$	$5.64^{+0.25}_{-0.17}$	$-1.76^{+0.20}_{-0.08}$			$1.16^{+0.21}_{-0.21}$	164.3	$\frac{155.9}{122}$
									159.6	$\frac{147.0}{120}$
[25,30]					$-0.57^{+0.05}_{-0.07}$	$-3.39^{+0.40}_{-0.30}$	$255.8^{+21.7}_{-18.1}$	$2.86^{+0.13}_{-0.13}$	123.0	$\frac{114.6}{122}$
	$-0.06^{+0.11}_{-0.13}$	$6.1^{+1.3}_{-0.8}$	$142.3^{+11.4}_{-11.4}$	$2.67^{+0.08}_{-0.14}$	$-0.61^{+0.05}_{-0.05}$		$271.4^{+15.0}_{-15.0}$	$2.65^{+0.12}_{-0.09}$	122.3	$\frac{116.0}{123}$
	$-0.60^{+0.49}_{-0.22}$	$14.7^{+1.7}_{-1.7}$	$237.5^{+36.7}_{-50.1}$	$2.61^{+0.23}_{-0.23}$	$-1.80^{+0.15}_{-0.41}$			$1.07^{+0.13}_{-0.27}$	126.1	$\frac{117.7}{122}$
									118.2	$\frac{105.6}{120}$
[30,35]					$-0.51^{+0.26}_{-0.24}$	$-2.25^{+0.30}_{-2.20}$	$114.5^{+21.4}_{-28.5}$	$0.94^{+0.09}_{-0.58}$	69.6	$\frac{61.2}{122}$
	$-0.85^{+0.12}_{-0.10}$	$7.2^{+0.8}_{-1.1}$	$597.4^{+332.5}_{-524.1}$	$1.03^{+0.30}_{-0.21}$	$-0.79^{+0.11}_{-0.15}$		$154.1^{+19.7}_{-23.6}$	$0.68^{+0.06}_{-0.06}$	73.9	$\frac{67.6}{123}$
	$-1.21^{+0.30}_{-0.15}$	$12.3^{+1.9}_{-1.9}$	$2277.6^{+1244.0}_{-1028.9}$	$0.65^{+0.32}_{-0.31}$	$-1.76^{+0.47}_{-0.02}$			$0.63^{+0.18}_{-0.18}$	81.9	$\frac{73.5}{122}$
									84.0	$\frac{71.4}{120}$
[35,50]					$-0.89^{+0.10}_{-0.17}$	$-2.46^{+0.30}_{-4.57}$	$118.3^{+28.1}_{-20.1}$	$0.56^{+0.05}_{-0.04}$	91.3	$\frac{82.9}{122}$
	$-0.61^{+0.17}_{-0.14}$	$4.3^{+0.9}_{-0.9}$	$125.0^{+12.4}_{-37.1}$	$0.51^{+0.04}_{-0.05}$	$-1.02^{+0.08}_{-0.10}$		$139.6^{+18.6}_{-16.3}$	$0.49^{+0.03}_{-0.04}$	92.7	$\frac{86.4}{123}$
	$-1.02^{+0.20}_{-0.10}$	$9.0^{+1.9}_{-2.0}$	$1841.1^{+1301.4}_{-1537.5}$	$0.43^{+0.30}_{-0.23}$	$-1.77^{+0.13}_{-0.11}$			$0.64^{+0.24}_{-1.29}$	89.7	$\frac{81.3}{122}$
									122.8	$\frac{110.2}{120}$

by probability NDP model (e.g., [Lundman et al. 2012](#)). To test this, we perform fit with NDP model³ on the spectrum of $T_0 + [-2, 15]$ s. In this procedure, we use a uniform jet with angle-independent baryon loading⁴. Therefore, there are only three parameters r_0 , η and L_w . The fit results is determined to be $\log r_0 = 8.35^{+0.03}_{-0.03}$ cm, $\eta = 227.2^{+100.5}_{-90.3}$ and $\log L_w = 49.67^{+0.02}_{-0.02}$ erg s $^{-1}$ with BIC=73.4. The spectrum is well described by the NDP model as shown in Figure 7 (b). The fit quality is even better than that of mBB model with Δ BIC of 2.2 and a larger freedom degree (BIC is 75.6 and a freedom degree of 122 with mBB model, as shown in Table. 3).

$1 + \sigma_0$ does not behave an evident increasing trend with time, which implies the possible Poynting flux is not increasing with time, even if it does exist; thus, small NT emission (as shown in Figure 4 (b) in blue triangles) in the tail of prompt phase ($> T_0 + 30$ s) is also likely from IS mechanism.

6. CONCLUSION AND SUMMARY

³ The details of probability NDP model is described in the Appendix B.

⁴ In the modeling with NDP model in this analysis, we find the extracted values of p and θ_c are large with large uncertainties, where p is the power-law index of the angle-dependent baryon loading and θ_c is the opening angle of the jet. Thus, a uniform jet is assumed, and there are three float parameters (η_0 , L and r_0) in the model.

⁵ Note this wind luminosity is that in which the probability emission of photons and an opening angle $\sim 5/\eta$ are considered.

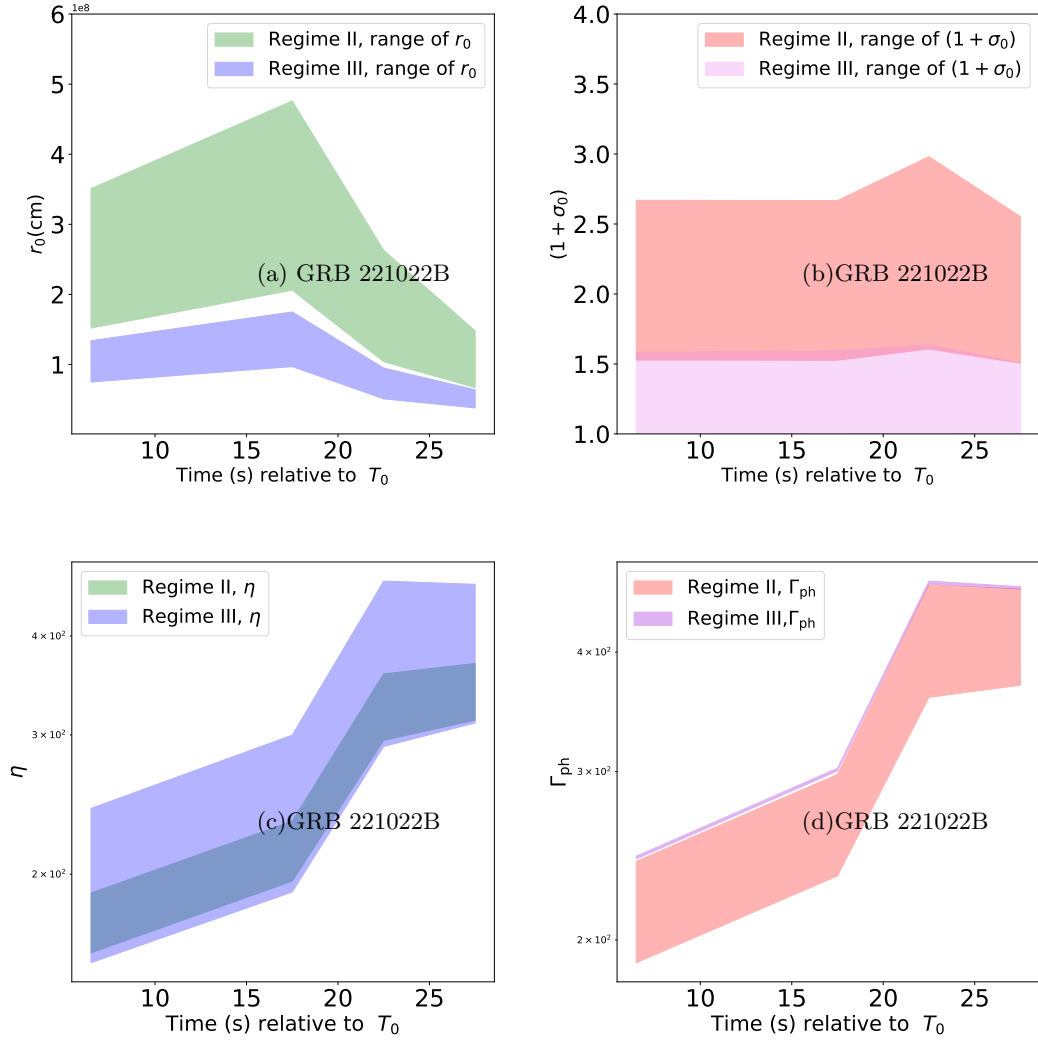


Figure 6. The ranges of r_0 , $(1 + \sigma_0)$, η , Γ_{ph} with $Y = 2$ in GRB 221022B.

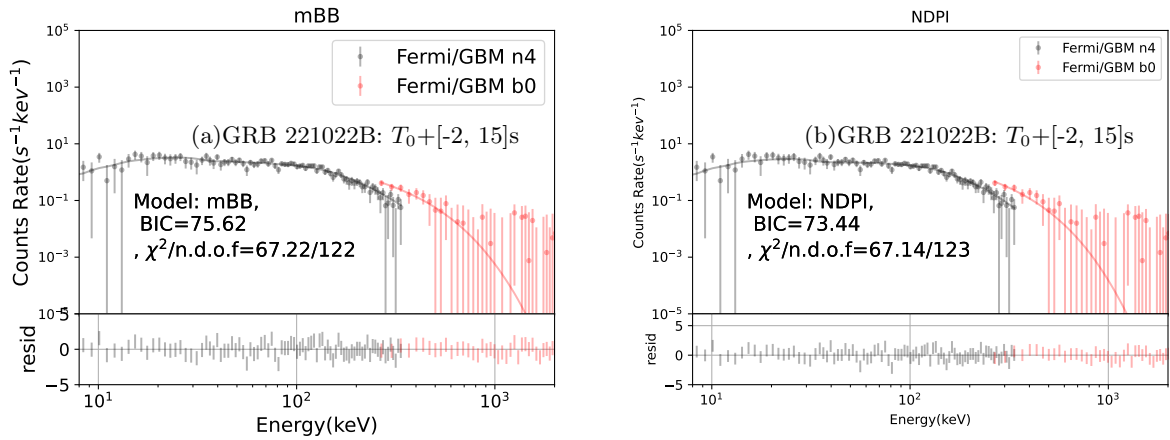


Figure 7. Spectra and fit results with different models in $T_0 + [-2, 15]$ s in GRB 221022B.

For the QT-dominated emission of which the spectrum is not hump-like, mBB or mBB+NT may be the preferred model than BB+NT in the modeling to the spectrum, as proved in this analysis. To diagnose the magnetization of the outflow with ‘top-down’ approach, we use a characteristic temperature with the corresponding flux from modeling with mBB or mBB+NT models. The magnetization parameter σ_0 as well as other parameters of the central engine could be constrained within narrower ranges, compared with those estimated with arbitrary values $r_0 = 10^7 - 10^9$ cm before. Moreover, the estimations with our method may provide more reasonable physical explanations. Note that if we find in a modeling, BB+BAND model has a better BIC or better physical explanation, we will take BB+BAND. This is not an absolute criterion.

GRB 221022B is a long burst dominated by the QT emission. Its prompt emission behaves a typical evolution from thermal to non-thermal, which may be a representative for some bursts. The fireball and hybrid outflow are both discussed as the possible origins for the prompt emission of GRB 221022B. From our analysis, it is proposed that the outflow for GRB 221022B is matter-flux-dominated. The preferred physical model for the early emission in the first 17 s spectra is NDP model, which is also consistent with this conclusion. Around the peak flux and the tail of the prompt phase, the NT emission is thought to be likely caused by IS mechanism, because of the increasing Lorentz Factor with time and small $(1 + \sigma_{15})$.

APPENDIX

A. MAGNETIZATION PARAMETERS IN CASE IIA

We derive relevant parameters in each regime, including r_{ra} and r_c (which are useful to write down the Γ evolution of the system), along with the photosphere properties, i.e. r_{ph} , Γ_{ph} , $(1 + \sigma_{\text{ph}})$, kT_{ob} , and F_{BB} (Gao & Zhang 2015) as below:

Regime I:

$$\begin{aligned}
r_{\text{ra}} &= 1.0 \times 10^{11} \text{ cm } r_{0,9} \eta_2, \\
r_c &= 1.0 \times 10^{17} \text{ cm } r_{0,9} \eta_2 (1 + \sigma_0)_2^3, \\
r_{\text{ph}} &= 8.34 \times 10^{10} \text{ cm } L_{w,52}^{1/3} r_{0,9}^{2/3} \eta_2^{-1/3} (1 + \sigma_0)_2^{-1/3}, \\
\Gamma_{\text{ph}} &= 83.4 L_{w,52}^{1/3} r_{0,9}^{-1/3} \eta_2^{-1/3} (1 + \sigma_0)_2^{-1/3}, \\
1 + \sigma_{\text{ph}} &= 100(1 + \sigma_0)_2, \\
kT_{\text{ob}} &= 56.1 \text{ keV } (1 + z)^{-1} L_{w,52}^{1/4} r_{0,9}^{-1/2} (1 + \sigma_0)_2^{-1/4}, \\
F_{\text{BB}} &= 1.07 \times 10^{-7} \text{ erg s}^{-1} \text{ cm}^{-2} L_{w,52} (1 + \sigma_0)_2^{-1} d_{L,28}^{-2}.
\end{aligned} \tag{A1}$$

Regime II:

$$\begin{aligned}
r_{\text{ra}} &= 1.0 \times 10^{11} \text{ cm } r_{0,9} \eta_2, \\
r_c &= 1.0 \times 10^{17} \text{ cm } r_{0,9} \eta_2 (1 + \sigma_0)_2^3, \\
r_{\text{ph}} &= 7.22 \times 10^{10} \text{ cm } L_{w,52}^{3/5} r_{0,9}^{2/5} \eta_2^{-7/5} (1 + \sigma_0)_2^{-3/5}, \\
\Gamma_{\text{ph}} &= 89.7 L_{w,52}^{1/5} r_{0,9}^{-1/5} \eta_2^{1/5} (1 + \sigma_0)_2^{-1/5}, \\
1 + \sigma_{\text{ph}} &= 17.7 L_{w,52}^{-1/5} r_{0,9}^{1/5} \eta_2^{4/5} (1 + \sigma_0)_2^{6/5}, \\
kT_{\text{ob}} &= 64.8 \text{ keV } (1 + z)^{-1} L_{w,52}^{-1/60} r_{0,9}^{-7/30} \eta_2^{16/15} (1 + \sigma_0)_2^{1/60}, \\
F_{\text{BB}} &= 1.24 \times 10^{-7} \text{ erg s}^{-1} \text{ cm}^{-2} L_{w,52}^{11/15} r_{0,9}^{4/15} \eta_2^{16/15} (1 + \sigma_0)_2^{-11/15} d_{L,28}^{-2}.
\end{aligned} \tag{A2}$$

Regime III:

$$\begin{aligned}
r_{\text{ra}} &= 1.0 \times 10^{11} \text{ cm } r_{0,9} \eta_2, \\
r_c &= 1.0 \times 10^{17} \text{ cm } r_{0,9} \eta_2 (1 + \sigma_0)_2^3, \\
r_{\text{ph}} &= 5.81 \times 10^{12} \text{ cm } L_{w,52} \eta_1^{-3} (1 + \sigma_0)_1^{-3}, \\
\Gamma_{\text{ph}} &= 100 \eta_1 (1 + \sigma_0)_1, \\
1 + \sigma_{\text{ph}} &\simeq 1, \\
kT_{\text{ob}} &= 6.65 \text{ keV } (1 + z)^{-1} L_{w,52}^{-5/12} r_{0,9}^{1/6} \eta_1^{8/3} (1 + \sigma_0)_1^{29/12}, \\
F_{\text{BB}} &= 7.15 \times 10^{-8} \text{ erg s}^{-1} \text{ cm}^{-2} L_{w,52}^{1/3} r_{0,9}^{2/3} \eta_1^{8/3} (1 + \sigma_0)_1^{5/3} d_{L,28}^{-2}.
\end{aligned} \tag{A3}$$

Regime IV:

(A4)

$$\begin{aligned}
r_{\text{ra}} &= 2.15 \times 10^{10} \text{ cm } r_{0,9} \eta_2^{1/3} (1 + \sigma_0)_2^{1/3}, \\
r_{\text{c}} &= 2.15 \times 10^{18} \text{ cm } r_{0,9} \eta_2^{7/3} (1 + \sigma_0)_2^{7/3}, \\
r_{\text{ph}} &= 8.34 \times 10^{10} \text{ cm } L_{w,52}^{1/3} r_{0,9}^{2/3} \eta_2^{-1/3} (1 + \sigma_0)_2^{-1/3}, \\
\Gamma_{\text{ph}} &= 83.4 L_{w,52}^{1/3} r_{0,9}^{-1/3} \eta_2^{-1/3} (1 + \sigma_0)_2^{-1/3}, \\
1 + \sigma_{\text{ph}} &= 5.56 L_{w,52}^{-1/3} r_{0,9}^{1/3} \eta_2^{4/3} (1 + \sigma_0)_2^{4/3}, \\
kT_{\text{ob}} &= 56.1 \text{ keV } (1 + z)^{-1} L_{w,52}^{1/4} r_{0,9}^{-1/2} (1 + \sigma_0)_2^{-1/4}, \\
F_{\text{BB}} &= 1.07 \times 10^{-7} \text{ erg s}^{-1} \text{ cm}^{-2} L_{w,52} (1 + \sigma_0)_2^{-1} d_{L,28}^{-2}.
\end{aligned}$$

(A5)

Regime V:

$$\begin{aligned}
r_{\text{ra}} &= 2.15 \times 10^{10} \text{ cm } r_{0,9} \eta_2^{1/3} (1 + \sigma_0)_2^{1/3}, \\
r_{\text{c}} &= 2.15 \times 10^{18} \text{ cm } r_{0,9} \eta_2^{7/3} (1 + \sigma_0)_2^{7/3}, \\
r_{\text{ph}} &= 2.46 \times 10^{11} \text{ cm } L_{w,52}^{3/5} r_{0,9}^{2/5} \eta_2^{-13/15} (1 + \sigma_0)_2^{-13/15}, \\
\Gamma_{\text{ph}} &= 48.5 L_{w,52}^{1/5} r_{0,9}^{-1/5} \eta_2^{-1/15} (1 + \sigma_0)_2^{-1/15}, \\
1 + \sigma_{\text{ph}} &= 17.7 L_{w,52}^{-1/5} r_{0,9}^{1/5} \eta_2^{16/15} (1 + \sigma_0)_2^{16/15}, \\
kT_{\text{ob}} &= 19.0 \text{ keV } (1 + z)^{-1} L_{w,52}^{-1/60} r_{0,9}^{-7/30} \eta_2^{8/15} (1 + \sigma_0)_2^{17/60}, \\
F_{\text{BB}} &= 3.63 \times 10^{-8} \text{ erg s}^{-1} \text{ cm}^{-2} L_{w,52}^{11/15} r_{0,9}^{4/15} \eta_2^{8/15} (1 + \sigma_0)_2^{-7/15} d_{L,28}^{-2}.
\end{aligned}$$

(A6)

Regime VI:

$$\begin{aligned}
r_{\text{ra}} &= 2.15 \times 10^{10} \text{ cm } r_{0,9} \eta_2^{1/3} (1 + \sigma_0)_2^{1/3}, \\
r_{\text{c}} &= 2.15 \times 10^{18} \text{ cm } r_{0,9} \eta_2^{7/3} (1 + \sigma_0)_2^{7/3}, \\
r_{\text{ph}} &= 5.81 \times 10^{12} \text{ cm } L_{w,52} \eta_1^{-3} (1 + \sigma_0)_1^{-3}, \\
\Gamma_{\text{ph}} &= 100 \eta_1 (1 + \sigma_0)_1, \\
1 + \sigma_{\text{ph}} &\simeq 1, \\
kT_{\text{ob}} &= 6.65 \text{ keV } (1 + z)^{-1} L_{w,52}^{-5/12} r_{0,9}^{1/6} \eta_1^{8/3} (1 + \sigma_0)_1^{29/12}, \\
F_{\text{BB}} &= 7.15 \times 10^{-8} \text{ erg s}^{-1} \text{ cm}^{-2} L_{w,52}^{1/3} r_{0,9}^{2/3} \eta_1^{8/3} (1 + \sigma_0)_1^{5/3} d_{L,28}^{-2}.
\end{aligned}$$

(A7)

B. THE MODELING OF GRB SPECTRUM

In this section, two empirical functions, including BAND and an exponential cut-off power law (CPL) functions are introduced, as well as the physical models, including multi-blackbody (mBB) function and non-dissipative photosphere (NDP) from pure hot fireball.

B.1. BAND function

The BAND function has four free parameters: low and high energy spectral indices, denoted as α and β respectively, the peak energy of νF_ν spectrum, denoted as E_p , and amplitude, as shown in Equation (B8) ($N(E)$ is in units of $\text{ph cm}^{-2} \text{ s}^{-1} \text{ keV}^{-1}$, the same below.).

$$N_{\text{BAND}}(E) = A \begin{cases} \left(\frac{E}{100 \text{ keV}}\right)^\alpha \exp\left[-\frac{(\alpha+2)E}{E_{\text{peak}}}\right], & E \geq \frac{(\alpha-\beta) E_{\text{peak}}}{\alpha+2} \\ \left(\frac{E}{100 \text{ keV}}\right)^\beta \exp(\beta - \alpha) \left[\frac{(\alpha-\beta)E_{\text{peak}}}{100 \text{ keV} (\alpha+2)}\right]^{\alpha-\beta}, & \\ E < \frac{(\alpha-\beta) E_{\text{peak}}}{\alpha+2}. \end{cases} \quad (\text{B8})$$

B.2. CPL model

CPL model is a subset of BAND model if β is very small and the part of $E < \frac{(\alpha-\beta) E_p}{\alpha+2}$ of BAND model is ignored. There are three parameters in CPL model: the amplitude A , the lower energy index α , and the νF_ν peak energy, E_p , as shown in Equation (B9).

$$N_{\text{COMP}}(E) = A \left(\frac{E}{1 \text{ keV}}\right)^\alpha \exp\left[-\frac{(\alpha+2) E}{E_p}\right]. \quad (\text{B9})$$

B.2.1. mBB model

the photon spectrum of the mBB can be formulated as

$$N(E) = \frac{8.0525(m+1)K}{\left[\left(\frac{T_{\text{max}}}{T_{\text{min}}}\right)^{m+1} - 1\right]} \left(\frac{kT_{\text{min}}}{\text{keV}}\right)^{-2} I(E), \quad (\text{B10})$$

where

$$I(E) = \left(\frac{E}{kT_{\text{min}}}\right)^{m-1} \int_{\frac{E}{kT_{\text{max}}}}^{\frac{E}{kT_{\text{min}}}} \frac{x^{2-m}}{e^x - 1} dx, \quad (\text{B11})$$

and $x = E/kT$; $K = L_{39}/D_{L,10\text{kpc}}^2$ is defined by the blackbody luminosity L in units of 10^{39} erg s $^{-1}$ in the GRB host galaxy frame and the luminosity distance D_L in units of 10 kpc; m is the power-law index of the distribution, and the temperature ranges from the minimum T_{min} to the maximum T_{max} .

B.3. NDP of pure fireball

The time-averaged flux $F_\nu(E_{\text{obs}}, r_0, \eta_0, p, \theta_c, \theta_\nu, L, z)$ of the observed energy E_{obs} is defined as

$$F_\nu(E_{\text{obs}}, r_0, \eta_0, p, \theta_c, \theta_\nu, L, z), \quad (\text{B12})$$

where r_0 is the acceleration radius measured at the base of the outflow, which is the radius where the acceleration of plasma to relativistic (kinetic) motion begins (Lundman et al. 2012; Pe'er et al. 2015). In the angle-dependent baryon loading parameter profile $\eta(\theta) \sim \frac{\eta_0}{((\theta/\theta_c)^{2p+1})^{1/2}}$, θ is the angle measured from the jet axis, p is the power-law index and $\eta_0 = \eta(\theta = 0)$. If the emission is from the saturated regime ($R_{\text{ph}} \geq R_s$, R_{ph} is the radius of photosphere and R_s is the saturation radius), $\Gamma = \eta$, otherwise, $\Gamma = R_{\text{ph}}/r_0$. θ_ν is the line of sight (LOS) measured from the jet axis. θ_c is the half-opening angle for the jet core. L is the entire outflow luminosity. z is the redshift.

R_{ph} in different regimes is defined as

$$R_{\text{ph}} = \begin{cases} \left(\frac{\sigma_T}{6m_p c} \frac{d\dot{M}}{d\Omega} r_0^2\right)^{1/3}, & R_{\text{ph}} \ll R_s, \\ \left(\frac{\sigma_T}{2m_p c} \frac{d\dot{M}}{d\Omega} r_0^2\right)^{1/3}, & R_{\text{ph}} \lesssim R_s, \\ \frac{1}{(1+\beta)\eta^2} \frac{\sigma_T}{m_p c} \frac{d\dot{M}}{d\Omega}, & R_{\text{ph}} \geq R_s, \end{cases} \quad (\text{B13})$$

and Γ in different regimes are determined to be

$$\Gamma = \begin{cases} R_{\text{ph}}/r_0, & R_{\text{ph}} < R_s, \\ \eta, & R_{\text{ph}} \geq R_s, \end{cases} \quad (\text{B14})$$

where β is the velocity, and $d\dot{M}(\theta)/d\Omega = L/4\pi c^2 \eta(\theta)$ is the angle-dependent mass outflow rate per solid angle, m_p is the mass of the proton, c is the light speed, and σ_T is electron Thomson cross section. In this analysis, we assume the jet is viewed on-axis to perform the fit, thus, $\theta_v = 0$ for this bright burst. $\theta_v = 0$ is a good approximation for small θ_v , i.e., θ_v is much less than the jet opening angle, as discussed in Lundman et al. (2012). There is a critical angle θ_{cri} , and the regime turns from unsaturated to saturated for $\theta > \theta_{\text{cri}}$, where θ is the angle measured from the jet axis. In the fitting procedure, an intermediate photosphere (Song et al. 2022b) is always considered, in which θ_{cri} is determined by the extracted parameters from the fit. If $\theta_{\text{cri}} \gtrsim 5/\eta_0$, the prompt emission is dominantly from the unsaturated regime (Lundman et al. 2012).

REFERENCES

- Beloborodov, A. M. 2013, *ApJ*, 764, 157, doi: [10.1088/0004-637X/764/2/157](https://doi.org/10.1088/0004-637X/764/2/157)
- Burgess, J. M. 2014, *MNRAS*, 445, 2589, doi: [10.1093/mnras/stu1925](https://doi.org/10.1093/mnras/stu1925)
- Cavallo, G., & Rees, M. J. 1978, *MNRAS*, 183, 359, doi: [10.1093/mnras/183.3.359](https://doi.org/10.1093/mnras/183.3.359)
- Chang, X.-Z., Lü, H.-J., Yang, X., Chen, J.-M., & Liang, E.-W. 2023, *ApJ*, 943, 146, doi: [10.3847/1538-4357/aca969](https://doi.org/10.3847/1538-4357/aca969)
- Chen, J.-M., Peng, Z.-Y., Du, T.-T., & Yin, Y. 2022, *ApJ*, 932, 25, doi: [10.3847/1538-4357/ac6c2a](https://doi.org/10.3847/1538-4357/ac6c2a)
- Gao, H., & Zhang, B. 2015, *ApJ*, 801, 103, doi: [10.1088/0004-637X/801/2/103](https://doi.org/10.1088/0004-637X/801/2/103)
- Giannios, D. 2006, *A&A*, 457, 763, doi: [10.1051/0004-6361:20065000](https://doi.org/10.1051/0004-6361:20065000)
- Giannios, D., & Spruit, H. C. 2005, *A&A*, 430, 1, doi: [10.1051/0004-6361:20047033](https://doi.org/10.1051/0004-6361:20047033)
- Goodman, J. 1986, *ApJL*, 308, L47, doi: [10.1086/184741](https://doi.org/10.1086/184741)
- Granot, J., Komissarov, S. S., & Spitkovsky, A. 2011, *MNRAS*, 411, 1323, doi: [10.1111/j.1365-2966.2010.17770.x](https://doi.org/10.1111/j.1365-2966.2010.17770.x)
- Hou, S.-J., Zhang, B.-B., Meng, Y.-Z., et al. 2018, *ApJ*, 866, 13, doi: [10.3847/1538-4357/aadc07](https://doi.org/10.3847/1538-4357/aadc07)
- Iyyani, S., Ryde, F., Axelsson, M., et al. 2013, *MNRAS*, 433, 2739, doi: [10.1093/mnras/stt863](https://doi.org/10.1093/mnras/stt863)
- Lloyd, N. M., & Petrosian, V. 2000, *ApJ*, 543, 722, doi: [10.1086/317125](https://doi.org/10.1086/317125)
- Lundman, C., Pe'er, A., & Ryde, F. 2012, *MNRAS*, 428, 2430, doi: [10.1093/mnras/sts219](https://doi.org/10.1093/mnras/sts219)
- Lundman, C., Pe'er, A., & Ryde, F. 2013, *MNRAS*, 428, 2430, doi: [10.1093/mnras/sts219](https://doi.org/10.1093/mnras/sts219)
- Meng, Y.-Z., Geng, J.-J., & Wu, X.-F. 2022, *MNRAS*, 509, 6047, doi: [10.1093/mnras/stab3132](https://doi.org/10.1093/mnras/stab3132)
- Mészáros, P., & Rees, M. J. 1997, *ApJL*, 482, L29, doi: [10.1086/310692](https://doi.org/10.1086/310692)
- Ohno, M., Ripa, J., Takahashi, H., et al. 2021, *GRB Coordinates Network*, 30697, 1
- Paczynski, B. 1986, *ApJL*, 308, L43, doi: [10.1086/184740](https://doi.org/10.1086/184740)
- Pe'er, A. 2008, *ApJ*, 682, 463, doi: [10.1086/588136](https://doi.org/10.1086/588136)
- Pe'er, A., Barlow, H., O'Mahony, S., et al. 2015, *ApJ*, 813, 127, doi: [10.1088/0004-637X/813/2/127](https://doi.org/10.1088/0004-637X/813/2/127)
- Pe'er, A., Ryde, F., Wijers, R. A. M. J., Mészáros, P., & Rees, M. J. 2007, *ApJL*, 664, L1, doi: [10.1086/520534](https://doi.org/10.1086/520534)
- Piran, T., Shemi, A., & Narayan, R. 1993, *MNRAS*, 263, 861, doi: [10.1093/mnras/263.4.861](https://doi.org/10.1093/mnras/263.4.861)
- Poolakkil, S., Meegan, C., & Fermi GBM Team. 2022, *GRB Coordinates Network*, 32830, 1
- Preece, R. D., Briggs, M. S., Mallozzi, R. S., et al. 1998, *ApJL*, 506, L23, doi: [10.1086/311644](https://doi.org/10.1086/311644)
- Rees, M. J., & Mészáros, P. 2005, *ApJ*, 628, 847, doi: [10.1086/430818](https://doi.org/10.1086/430818)
- Ridnaia, A., Frederiks, D., Lysenko, A., et al. 2022, *GRB Coordinates Network*, 32109, 1
- Ryde, F., Axelsson, M., Zhang, B. B., et al. 2010, *ApJL*, 709, L172, doi: [10.1088/2041-8205/709/2/L172](https://doi.org/10.1088/2041-8205/709/2/L172)
- Scargle, J. D., Norris, J. P., Jackson, B., & Chiang, J. 2013, *ApJ*, 764, 167, doi: [10.1088/0004-637X/764/2/167](https://doi.org/10.1088/0004-637X/764/2/167)
- Song, X.-Y., & Meng, Y.-Z. 2022, *MNRAS*, 512, 5693, doi: [10.1093/mnras/stac839](https://doi.org/10.1093/mnras/stac839)
- Song, X.-Y., Zhang, S.-N., Zhang, S., Xiong, S.-L., & Song, L.-M. 2022a, *ApJ*, 931, 112, doi: [10.3847/1538-4357/ac6b33](https://doi.org/10.3847/1538-4357/ac6b33)
- . 2022b, *ApJ*, 931, 112, doi: [10.3847/1538-4357/ac6b33](https://doi.org/10.3847/1538-4357/ac6b33)
- Vlahakis, N., & Königl, A. 2003, *ApJ*, 596, 1104, doi: [10.1086/378227](https://doi.org/10.1086/378227)
- Vurm, I., Beloborodov, A. M., & Poutanen, J. 2011, *ApJ*, 738, 77, doi: [10.1088/0004-637X/738/1/77](https://doi.org/10.1088/0004-637X/738/1/77)
- Wang, X. I., Zheng, X., Xiao, S., et al. 2021, *ApJ*, 922, 237, doi: [10.3847/1538-4357/ac29bd](https://doi.org/10.3847/1538-4357/ac29bd)
- Wei, J.-J., Wu, X.-F., & Melia, F. 2016, *MNRAS*, 463, 1144, doi: [10.1093/mnras/stw2057](https://doi.org/10.1093/mnras/stw2057)
- Zhang, B., Lu, R.-J., Liang, E.-W., & Wu, X.-F. 2012, *ApJL*, 758, L34, doi: [10.1088/2041-8205/758/2/L34](https://doi.org/10.1088/2041-8205/758/2/L34)
- Zhang, B., & Yan, H. 2011, *ApJ*, 726, 90, doi: [10.1088/0004-637X/726/2/90](https://doi.org/10.1088/0004-637X/726/2/90)
- Zhang, B. B., Zhang, B., Sun, H., et al. 2018, *Nature Communications*, 9, 447, doi: [10.1038/s41467-018-02847-3](https://doi.org/10.1038/s41467-018-02847-3)